

# Tin-Based Chalcogenide Perovskites: A Promising Lead-Free Alternative for Stable and High-Performance Photovoltaics

Surajit Adhikari\*, Sankhasuvra Das, and Priya Johari\*  
*Department of Physics, School of Natural Sciences,  
Shiv Nadar Institution of Eminence, Greater Noida,  
Gautam Buddha Nagar, Uttar Pradesh 201314, India.*

Chalcogenide perovskites (CPs) have sparked interest as promising optoelectronic materials due to their stability, nontoxicity, small bandgaps, large absorption coefficients, and high defect tolerance. Here, using state-of-the-art first-principles-based density functional theory, density functional perturbation theory, and many-body perturbation theory (i.e., GW and BSE), we explicate the excitonic and polaronic phenomena as well as the relative stability and optoelectronic properties in a series of distorted CPs  $\text{ASnX}_3$  ( $A = \text{Ca, Sr, Ba}$ ;  $X = \text{S, Se}$ ). Our findings reveal that these perovskites are mechanically stable and exhibit direct  $G_0W_0$  bandgaps ranging from 0.79 to 1.50 eV. Moreover, we find that the exciton binding energy of these compounds (0.04–0.23 eV) is comparable to that of Zr- and Hf-based CPs but little higher than that of conventional lead halide perovskites (HPs). Additionally, we look into polaron-facilitated charge carrier mobility for electrons ( $21.33\text{--}416.02 \text{ cm}^2\text{V}^{-1}\text{s}^{-1}$ ) and holes ( $7.02\text{--}260.69 \text{ cm}^2\text{V}^{-1}\text{s}^{-1}$ ), which are comparable to or higher than those observed in lead HPs and significantly exceed those in Zr- and Hf-based CPs, owing to reduced carrier-phonon couplings in the former. Finally, the estimated spectroscopic limited maximum efficiency (24.2%–31.2%) reflects that they can be promising candidates for photovoltaic applications. This has been further confirmed by assessing the performance of perovskite solar cells through conventional device (FTO/ $\text{TiO}_2$ / $\text{ASnX}_3$ /Spiro-OMeTAD/Au) simulations using SCAPS-1D software.

## I. INTRODUCTION:

Chalcogenide perovskites (CPs)[1–4] have recently been emerged as a potential alternatives for the high-performing inorganic-organic halide perovskites (IOHPs)[5–8]. While IOHPs face significant obstacles for their large-scale industrial applications owing to the toxicity of lead and instability due to the presence of organic cations[9, 10], CPs show promise because of their vast availability in the earth’s crust, non-toxic nature, and exceptional stability[1, 11–13]. In addition to these advantages, CPs exhibit favorable characteristics such as small electronic bandgap, high absorption coefficient, promising defect tolerance, good charge carrier mobility, and excellent power conversion efficiency (PCE)[2–4, 14, 15], which point toward their potential application in a variety of optoelectronic devices.

Similar to the typical three-dimensional halide perovskites (HPs), the chemical formula of chalcogenide perovskites is expressed as  $\text{ABX}_3$ [4, 16], where A and B stand for divalent alkali-earth metal cations ( $\text{Ca}^{2+}$ ,  $\text{Sr}^{2+}$ ,  $\text{Ba}^{2+}$ ) and tetravalent transition metal cations ( $\text{Ti}^{4+}$ ,  $\text{Zr}^{4+}$ ,  $\text{Hf}^{4+}$ , and  $\text{Sn}^{4+}$ ), respectively, and X is typically a chalcogen anion such as  $\text{S}^{2-}$  or  $\text{Se}^{2-}$ . Numerous experimental and theoretical investigations have demonstrated the successful synthesis of chalcogenide perovskites and unveiled their intriguing properties[1–4, 11–14, 17, 18]. For example, Lelieveld et al.[17] had synthesized the distorted phase of  $\text{CaZrS}_3$ ,  $\text{SrZrS}_3$ ,  $\text{BaZrS}_3$ ,  $\text{CaHfS}_3$ ,  $\text{SrHfS}_3$ , and  $\text{BaHfS}_3$  in 1980, while later, the needle-like phase[18–20] of  $\text{SrZrS}_3$ ,  $\text{SrZrSe}_3$ , and  $\text{SrHfSe}_3$  CPs were also synthesized by various groups in the end of 20<sup>th</sup> century and beginning of 21<sup>st</sup> century. In 2016, Perera et al.[21] used high-temperature sulfurization of the oxides with  $\text{CS}_2$  to synthesize  $\text{AZrS}_3$  ( $A = \text{Ba, Ca, and Sr}$ ). On the other hand, in 2015, Sun et al.[4] theoretically affirmed the formation of two distinct phases of CPs at room temperature: the needle-like phase ( $\text{NH}_4\text{CdCl}_3$ -type) and the distorted phase ( $\text{GdFeO}_3$ -type), both sharing the orthorhombic structure with same space group  $Pnma$  (No. 62), and predicted them to be promising for application in solar cells. In addition, several first-principles DFT-based studies have been conducted, indicating that CPs exhibit interesting electronic and optical properties suitable for use in photovoltaic applications[4, 14–16, 22].

Several studies have primarily focused on Zr- and Hf-based CPs[14, 15, 22], which demonstrate exciton binding energies ranging from 0.02 to 0.26 eV, comparable to or higher than those observed in conventional HPs (0.01–0.10 eV)[23–25]. However, the main drawback of Zr- and Hf-based CPs lies in their reduced charge carrier mobility ( $6.84\text{--}77.59 \text{ cm}^2\text{V}^{-1}\text{s}^{-1}$ ) and lower PCE (10.56%–25.02%) compared to conventional HPs, which have charge carrier

---

\* sa731@snu.edu.in, priya.johari@snu.edu.in

mobility and PCE in the range of 57–290  $\text{cm}^2\text{V}^{-1}\text{s}^{-1}$  [26, 27] and 21.15%–28.97% [28, 29], respectively. These limitations are majorly due to prominent polaronic effects, which hinder their effectiveness for solar cell applications. This makes exploration of alternatives for the B-site cation even more crucial in order to achieve high polaronic charge carrier mobility along with high PCE, thereby, enhancing the effectiveness of CPs for the solar cell applications.

Recent first-principles calculations highlight the potential of Sn as B-site cation *via* distorted  $\text{SrSnX}_3$  ( $X = \text{S, Se}$ ) perovskites as promising photovoltaic materials solely based on their electronic and optical properties upto the HSE06 level [30, 31]. Experimental investigations have further substantiated this potential by successfully fabricating distorted  $\text{CaSnS}_3$  perovskite at 500°C [32]. Basera et al. [14] have furthermore provided valuable insights into the photovoltaic properties of distorted  $\text{CaSnS}_3$ , as well as needle-like phases of  $\text{BaSnS}_3$  and  $\text{SrSnS}_3$  perovskites. However, the challenge posed by these needle-like CPs lies in their higher bandgap (1.91–2.04 eV) and lower theoretical efficiency (21.80%). While, in contrast, the bandgap of distorted  $\text{CaSnS}_3$  falls within the optimal range at 1.43 eV, with theoretical efficiency reaching up to 32.45% [14]. Motivated by these findings, we aim to conduct a comprehensive theoretical analysis of distorted Sn-based chalcogenides to elucidate their photovoltaic application suitable features.

Henceforth, our endeavor has been to meticulously explore the optoelectronic, transport, excitonic, and polaronic properties of distorted Sn-based,  $\text{ASnX}_3$  ( $A = \text{Ca, Sr, Ba}$ ;  $X = \text{S, Se}$ ) chalcogenide perovskites utilizing a combination of density functional theory (DFT) [33, 34], density functional perturbation theory (DFPT) [35], and advanced many-body perturbation theory based methodologies like GW and BSE [36, 37]. Initially, the crystal structures are optimized using semilocal PBE [38] exchange–correlation (xc) functional, and their stability has been examined. The electronic properties of the relaxed structures are calculated using HSE06 [39] xc functional as well as  $G_0W_0$ @PBE [40, 41] methodology. The investigated CPs exhibit direct bandgaps ranging from 0.79 to 1.50 eV, which fall within the optimal range when compared to most lead-based HPs [23, 24, 28] as well as Zr- and Hf-based CPs [14, 15, 22]. Following this, optical properties and exciton binding energies ( $E_B$ ) are determined through the Bethe-Salpeter equation (BSE) [42, 43] method. Furthermore, employing the DFPT technique, the ionic contribution to the dielectric function is computed, and the Fröhlich model is invoked to evaluate polaronic attributes such as carrier-phonon coupling strength and polaron mobility (21.33–416.02  $\text{cm}^2\text{V}^{-1}\text{s}^{-1}$ ). Conclusively, the estimation of the spectroscopic limited maximum efficiency (SLME) [44] between 24.20%–31.20% utilizing the quasiparticle (QP) bandgap and absorption coefficient underscores  $\text{ASnX}_3$  as a material with significant potential for photovoltaic applications. This has been further confirmed by performing the conventional device (FTO/ $\text{TiO}_2$ / $\text{ASnX}_3$ /Spiro-OMeTAD/Au) simulations using SCAPS-1D software [45–48].

## II. COMPUTATIONAL METHODOLOGIES AND NUMERICAL SIMULATIONS:

### A. Computational Details:

In this work, the state-of-the-art first-principles calculations based on density functional theory (DFT) [33, 34], density functional perturbation theory (DFPT) [35], and many-body perturbation theory (MBPT) [36, 37] were performed using the Vienna Ab initio Simulation Package (VASP) [49, 50]. In all constituent elements, the valence electrons and atomic core interactions were described using the projector-augmented wave (PAW) pseudopotentials [51]. The PAW pseudopotentials with valence-electron configurations considered for Ca, Sr, Ba, Sn, S, and Se were  $3s^23p^64s^2$ ,  $4s^24p^65s^2$ ,  $5s^25p^66s^2$ ,  $4d^{10}5s^25p^2$ ,  $3s^23p^4$ , and  $4s^24p^4$ , respectively. For the structural optimization, the generalized gradient approximation (GGA) [38] based exchange–correlation (xc) functional of Perdew, Burke, and Ernzerhof (PBE) was employed, which takes into account the electron–electron interactions. The plane-wave cutoff energy was set to 400 eV, and the electronic self-consistent-field iteration energy convergence threshold was chosen as  $10^{-6}$  eV. The lattice constants and coordinates of all the atoms were fully optimized until the Hellmann-Feynman forces on each atom were less than 0.01 eV/Å. The  $\Gamma$ -centered  $7 \times 7 \times 5$   $\mathbf{k}$ -point sampling was used for Brillouin zone integration in order to determine the optimized structures. Visualization for Electronic and Structural Analysis (VESTA) [52] software package was used to display the optimized crystal structures.

The phonon spectra were calculated using the DFPT method as implemented in the PHONOPY [53] package by considering a  $2 \times 2 \times 2$  supercell. Since, GGA is known to underestimate the band gap, the electronic band structures were computed using the hybrid HSE06 [39] xc functional as well as many-body perturbation theory (MBPT) based  $G_0W_0$  [40, 41] ( $G_0W_0$ @PBE) method. Note that the spin-orbit coupling (SOC) effect was not considered as it does not impact the bandgap (for details, see the Supplemental Material) of the considered systems. The effective mass was computed by SUMO [54] using a parabolic fitting of the band edges. We also carried out Bethe-Salpeter equation (BSE) [42, 43] based calculations on top of the single-shot  $G_0W_0$ @PBE to precisely estimate the optical properties, which takes explicitly into account the electron-hole interaction. Here, a  $\Gamma$ -centered  $3 \times 3 \times 2$   $\mathbf{k}$ -grid and a converged 640 NBANDS were used for the GW-BSE calculations. The electron-hole kernel for the BSE calculations was generated by considering 24 occupied and 24 unoccupied bands. The VASPKIT [55] package was used to post-

process the elastic and optical properties. The ionic contribution to the dielectric constant was also calculated using the DFPT method.

Using the hydrogenic Wannier–Mott (WM)[22, 56] model, the exciton binding energy ( $E_B$ ) for a screened Coulomb interacting  $e - h$  pair is calculated as follows:

$$E_B = \left( \frac{\mu^*}{m_0 \varepsilon_{\text{eff}}^2} \right) R_\infty, \quad (1)$$

where,  $\mu^*$  represents the reduced mass of the charge carriers,  $m_0$  denotes the rest mass of electron,  $\varepsilon_{\text{eff}}$  is the effective dielectric constant, and  $R_\infty$  is the Rydberg constant.

The phonon screening correction to the exciton binding energy ( $E_B$ ) is given by[57]:

$$\Delta E_B^{ph} = -2\omega_{LO} \left( 1 - \frac{\varepsilon_\infty}{\varepsilon_{\text{static}}} \right) \frac{\sqrt{1 + \omega_{LO}/E_B} + 3}{\left( 1 + \sqrt{1 + \omega_{LO}/E_B} \right)^3}, \quad (2)$$

where,  $\varepsilon_\infty$  and  $\varepsilon_{\text{static}}$  are the electronic (optical) and static (electronic + ionic) dielectric constants, and  $\omega_{LO}$  is the characteristic phonon angular frequency. The thermal "B" approach of Hellwarth et al.[58] is used to determine  $\omega_{LO}$  by taking the spectral average of the multiple phonon branches (for details, see the SM).

Within the framework of Fröhlich's polaron model, the longitudinal optical phonons and the electron travelling through the lattice interact via the dimensionless Fröhlich parameter  $\alpha$ , which is expressed as[59],

$$\alpha = \frac{1}{4\pi\varepsilon_0} \frac{1}{2} \left( \frac{1}{\varepsilon_\infty} - \frac{1}{\varepsilon_{\text{static}}} \right) \frac{e^2}{\hbar\omega_{LO}} \left( \frac{2m^*\omega_{LO}}{\hbar} \right)^{1/2}, \quad (3)$$

where,  $\varepsilon_0$  is the permittivity of free space and  $m^*$  is the carrier effective mass. One can also estimate the polaron energy ( $E_p$ ) by knowing the value of  $\alpha$  using equation[14, 22]:

$$E_p = (-\alpha - 0.0123\alpha^2)\hbar\omega_{LO} \quad (4)$$

Feynman's extended version of Fröhlich's polaron theory (for a small  $\alpha$ ) is also used to obtain the effective mass of the polaron ( $m_p$ ) as follows[60]:

$$m_p = m^* \left( 1 + \frac{\alpha}{6} + \frac{\alpha^2}{40} + \dots \right) \quad (5)$$

Finally, using the Hellwarth polaron model[58], the polaron mobility is defined as follows:

$$\mu_p = \frac{(3\sqrt{\pi}e)}{2\pi c\omega_{LO}m^*\alpha} \frac{\sinh(\beta/2)}{\beta^{5/2}} \frac{w^3}{v^3} \frac{1}{K(a,b)} \quad (6)$$

where,  $e$  is the charge of electron,  $\beta = \hbar c\omega_{LO}/k_B T$ , and  $w$  and  $v$  are the temperature-dependent variational parameters, and  $K(a,b)$  is a function of  $\beta$ ,  $w$ , and  $v$  (for details, see the SM).

## B. SCAPS-1D Numerical Simulations:

SCAPS-1D software is utilized for conducting numerical device simulations on solar cells to assess their performance and aid in design optimization. The tool was developed by Prof. M. Burgelman at the Department of Electronics and Information Systems (ELIS) of the University of Gent, Belgium[61, 62]. SCAPS solves the Poisson's equation, which correlates the electrostatic potential to the overall charge density, along with continuity equations for electrons and holes in the conduction and valence bands, respectively. It can predict device characteristics such as current density-voltage curve, efficiency, energy bands, and other properties of the solar cell structure under illumination. Figure 5(a) shows the proposed perovskite solar cell (PSC) structure having the architecture of FTO/TiO<sub>2</sub>/Perovskite/Spiro-OMeTAD/Au. In this proposed structure, Spiro-OMeTAD is used as the hole transport layer (HTL), TiO<sub>2</sub> was

used as the electron transport layer (ETL), FTO (fluorine-doped tin oxide) as the transparent conducting oxide (TCO), and perovskite as the absorber layer. Gold (Au) having a work function of 5.1 eV was employed as the back metallic contact. The simulation parameters for the HTL, ETL and FTO, chosen based on theoretical and experimental results[45], are listed in Table S14 of the SM. Also, Table S15 shows the input parameters for the perovskite layer, estimated through our theoretical calculations (for details, see the SM). The simulations were conducted under the illumination of AM1.5G at 300K working temperature. The Poisson's equation and the continuity equations of both the carriers (electrons and holes) for SCAPS-1D simulation are written as[46, 47],

$$\frac{\partial^2 \psi}{\partial x^2} = -\frac{q}{\varepsilon}[p(x) - n(x) + N_D - N_A + \rho_p \rho_n] \quad (7)$$

$$-\left(\frac{1}{q}\right) \frac{\partial J_p}{\partial x} + G_{op} - R(x) = \frac{\partial p}{\partial t} \quad (8)$$

$$\left(\frac{1}{q}\right) \frac{\partial J_n}{\partial x} + G_{op} - R(x) = \frac{\partial n}{\partial t} \quad (9)$$

Here  $\psi$  is the electrostatic potential,  $\varepsilon$  is the permittivity of the material,  $p$  and  $n$  are electron and hole concentrations,  $N_D$  and  $N_A$  are donor and acceptor densities,  $J_n$  and  $J_p$  are electron and hole current densities,  $\rho_n$  and  $\rho_p$  are electron and hole distribution,  $R$  is the recombination and  $G_{op}$  is the optical generation rate.

The open circuit voltage ( $V_{oc}$ ) of the perovskite solar cell (PSC) is given by[45],

$$V_{oc} = \frac{nk_B T}{q} \ln\left(\frac{J_{sc}}{J_s} + 1\right) \quad (10)$$

where,  $J_{sc}$  is the short circuit current density and  $J_s$  is the reverse saturation current. The Fill Factor (FF) is given by[48]:

$$FF = \frac{P_{max}}{J_{sc} V_{oc}} \quad (11)$$

and the Power Conversion efficiency, PCE ( $\eta$ ) is defined as[48]:

$$\eta = \frac{P_{max}}{P_{in}} = \frac{FF \times J_{sc} \times V_{oc}}{P_{in}} \quad (12)$$

where,  $P_{max}$  is the maximum power of solar cell, and  $P_{in}$  is the input solar power equivalent to the AM1.5G Sun spectrum.

### III. RESULTS AND DISCUSSIONS:

In this study, we undertook a systematic and thorough investigation into the distorted phases of Sn-based chalcogenide perovskites  $\text{ASnX}_3$  (A = Ca, Sr, Ba; X = S, Se) with the aim of exploring their potential optoelectronic features. The subsequent sections delve into the stability as well as the structural, electronic properties, transport phenomena, optical properties, excitonic dynamics, polaronic effects, and the spectroscopic limited maximum efficiency (SLME) of  $\text{ASnX}_3$  chalcogenide perovskites. Through this detailed examination and discussion, our aim is to establish a foundational understanding and provide insights to guide future experimental endeavors.



### A. Structural Properties:

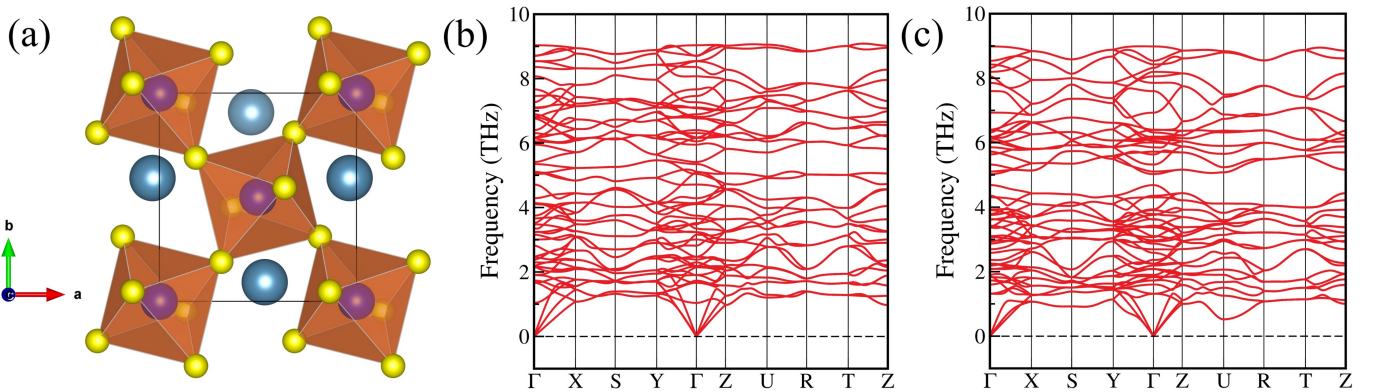


Figure 1. (a) Crystal structure of  $\text{CaSnS}_3$  in orthorhombic distorted phase, and phonon dispersion curves of (b)  $\text{SrSnS}_3$ , and (c)  $\text{BaSnS}_3$  calculated using DFPT method. Blue, purple, and yellow balls represent Ca, Sn, and S atoms, respectively.

The orthorhombic distorted crystal structure with the space group  $Pnma$  (No. 62)[17] of chalcogenide perovskites  $\text{ASnX}_3$  ( $A = \text{Ca, Sr, Ba}$ ;  $X = \text{S, Se}$ ) are presented in Figure 1(a) and Figure S1. The crystal structure of these compounds usually consists of four formula units, i.e., 20 atoms, of which 4 are Ca/Sr/Ba, 4 are Sn, and 12 are S or Se atoms. In this distorted phase, the alkaline earth elements (A-site cations) have 12-fold coordination, and they form cuboctahedrons with chalcogenides X (S or Se). On the other hand, the corner-sharing distorted octahedrons  $[\text{SnX}_6]^{8-}$  are produced due to the 6-fold coordination of Sn cation with X (S or Se) atoms in a distorted and tilted way. The lattice parameters and average bond lengths of the optimized crystal structures are calculated using the PBE xc functional and are tabulated in Table I and Table S1, respectively. It is found that the lattice parameters are in good agreement with previous theoretical and available experimental results[30, 32]. The crystallographic stability of these CPs is quantitatively identified by calculating the Goldschmidt tolerance factor ( $t$ ), the octahedral factor ( $\mu$ ), and the new tolerance factor ( $\tau$ )[56, 63, 64] (for details, see the SM). From Table S2, it can be noticed that the  $t$ ,  $\mu$ , and  $\tau$  values of these investigated CPs are in the range of 0.879–0.964, 0.348–0.375, and 4.174–4.721, respectively, confirming the reasonable structural stability of these distorted CPs[16, 63]. Furthermore, the decomposition energy is also calculated for these materials using the PBE xc functional to ascertain their thermodynamic stability (for details, see Table S3 of the SM). The negative decomposition energy reveals these perovskites to be unstable at 0 K, but, there remains a possibility for them to stabilize at higher temperatures, as also demonstrated by Hamza et al. by synthesizing  $\text{CaSnS}_3$  perovskite at  $500^\circ\text{C}$ [32], which is an indicator of their higher temperature stability. Further, the dynamical and mechanical stability of the studied CPs are examined.

Table I. Calculated lattice parameters of  $\text{ASnX}_3$  ( $A = \text{Ca, Sr, Ba}$ ;  $X = \text{S, Se}$ ) chalcogenide perovskites.

Configurations	This Work			Previous Work			Reference
	a (Å)	b (Å)	c (Å)	a (Å)	b (Å)	c (Å)	
$\text{CaSnS}_3$	6.71	7.08	9.67	6.69	7.08	11.29	Expt.[32]
$\text{SrSnS}_3$	6.90	7.22	9.82	6.90	7.21	9.84	Theo.[30]
$\text{BaSnS}_3$	7.04	7.27	10.17				
$\text{CaSnSe}_3$	7.06	7.47	10.15				
$\text{SrSnSe}_3$	7.24	7.62	10.29	7.25	7.61	10.31	Theo.[30]
$\text{BaSnSe}_3$	7.32	7.73	10.63				

In Figure 1(b)-(c), the phonon spectra of  $\text{SrSnS}_3$  and  $\text{BaSnS}_3$  CPs have been depicted, which validates their dynamical stability at 0 K. The rest of the compounds are found to be unstable at 0 K but they may become dynamically stable at higher temperatures, as discussed before. To investigate the mechanical stability, the second-order elastic coefficients ( $C_{ij}$ ) of these CPs are calculated using the energy-strain approach[65] (for details, see the SM). The computed  $C_{ij}$  values of these compounds are listed in Table S4, and they are found to satisfy the Born stability criteria[65]. Using these elastic coefficients, the bulk modulus ( $B$ ), shear modulus ( $G$ ), Young's modulus ( $Y$ ), and Poisson's ratio ( $\nu$ ) of these materials[66, 67] are investigated (for details, see the SM). The fragility of the materials is studied in terms of Pugh's suggested ratio ( $B/G$ )[68] and Poisson's ratio ( $\nu$ ). The calculated values of

$B/G$  ( $> 1.75$ ) and  $\nu$  ( $> 0.26$ ) reveal that the examined CPs are ductile in nature (see Table S4). Additionally, the longitudinal ( $v_l$ ), transverse ( $v_t$ ), and average ( $v_m$ ) elastic wave velocities and the Debye temperature ( $\Theta_D$ )[69] are calculated (see Table S5), as they hold crucial significance for flexible optoelectronic applications.

Table II. Bandgap (in eV) of chalcogenide perovskites. Here, Ca- and Sr-based CPs are direct bandgap materials, whereas Ba-based CPs are indirect bandgap materials. For Ba-based CPs,  $i$  and  $d$  represent indirect and direct bandgaps, respectively.

Configurations	PBE	HSE06	$G_0W_0@PBE$	Previous Work
CaSnS <sub>3</sub>	0.77	1.40	1.44	1.72 (Expt.[32])
SrSnS <sub>3</sub>	0.83	1.45	1.50	1.56 (Theo.[31])
BaSnS <sub>3</sub>	0.64 <sup><i>i</i></sup> (0.66 <sup><i>d</i></sup> )	1.16 <sup><i>i</i></sup> (1.23 <sup><i>d</i></sup> )	1.18 <sup><i>i</i></sup> (1.28 <sup><i>d</i></sup> )	
CaSnSe <sub>3</sub>	0.25	0.70	0.79	
SrSnSe <sub>3</sub>	0.42	0.86	0.88	1.00 (Theo.[31])
BaSnSe <sub>3</sub>	0.54 <sup><i>i</i></sup> (0.55 <sup><i>d</i></sup> )	0.93 <sup><i>i</i></sup> (1.00 <sup><i>d</i></sup> )	0.99 <sup><i>i</i></sup> (1.04 <sup><i>d</i></sup> )	

## B. Electronic Properties:

After examining the stability, the electronic properties, such as band structure and partial density of states (PDOS) of the chalcogenide perovskites  $ASnX_3$  ( $A = Ca, Sr, Ba; X = S, Se$ ) are computed to gain deep insights for designing the photoelectric devices. At first, the electronic band structure calculations are performed using the semi-local GGA-PBE xc functional with and without including the spin-orbit coupling (SOC) for these CPs. It is found that GGA-PBE xc functional is unable to predict the correct bandgaps due to the self-interaction error of the electrons (see Table II), and SOC does not have any impact on the bandgap (see Table S6 of the SM), which is expected for chalcogenide perovskites[14, 22]. After that, we employed the hybrid HSE06 xc functional and many-body perturbation theory (MBPT) based GW ( $G_0W_0@PBE$ ) method to calculate the bandgaps more accurately. The HSE06 and  $G_0W_0@PBE$  calculated band structures of these compounds are depicted in Figure 2 and Figure S3, respectively. Our results revealed that Ca- and Sr-based compounds have direct bandgaps at  $\Gamma$  (0, 0, 0) point, while Ba-based CPs exhibit indirect bandgaps. In the case of BaSnS<sub>3</sub> and BaSnSe<sub>3</sub>, the valence band maxima (VBM) are situated at the S (0.5, 0.5, 0) and U (0.5, 0, 0.5) points of the Brillouin zone (BZ), respectively, while the conduction band minima (CBM) are found in between  $\Gamma$  and X (0.5, 0, 0) point for both cases (see Figure 2). Also, both of them exhibit the lowest direct bandgap in between  $\Gamma$  and X point of the BZ. The HSE06 as well as  $G_0W_0@PBE$  estimated bandgaps of these CPs are listed in Table II, which closely match with earlier theoretical and available experimental findings. For example, the  $G_0W_0@PBE$  bandgap of CaSnS<sub>3</sub> (1.44 eV) closely aligns with its experimental bandgap of 1.72 eV[32]. The discrepancy in bandgap values could be attributed to the temperature, as the experimental bandgap was measured at 500° C. The HSE06 and  $G_0W_0@PBE$  computed bandgap of these CPs lie in the range of 0.70–1.45 eV and 0.79–1.50 eV, respectively. Thus, the bandgaps of the investigated CPs are within the ideal range for photovoltaic applications, aligning well with those of most lead-based HPs (1.50–3.13 eV)[23, 24, 28], as well as Zr- and Hf-based CPs (1.69–2.46 eV)[14, 15, 22] (for details, see Table S13 of the SM). This suggests their high suitability for photovoltaic applications.

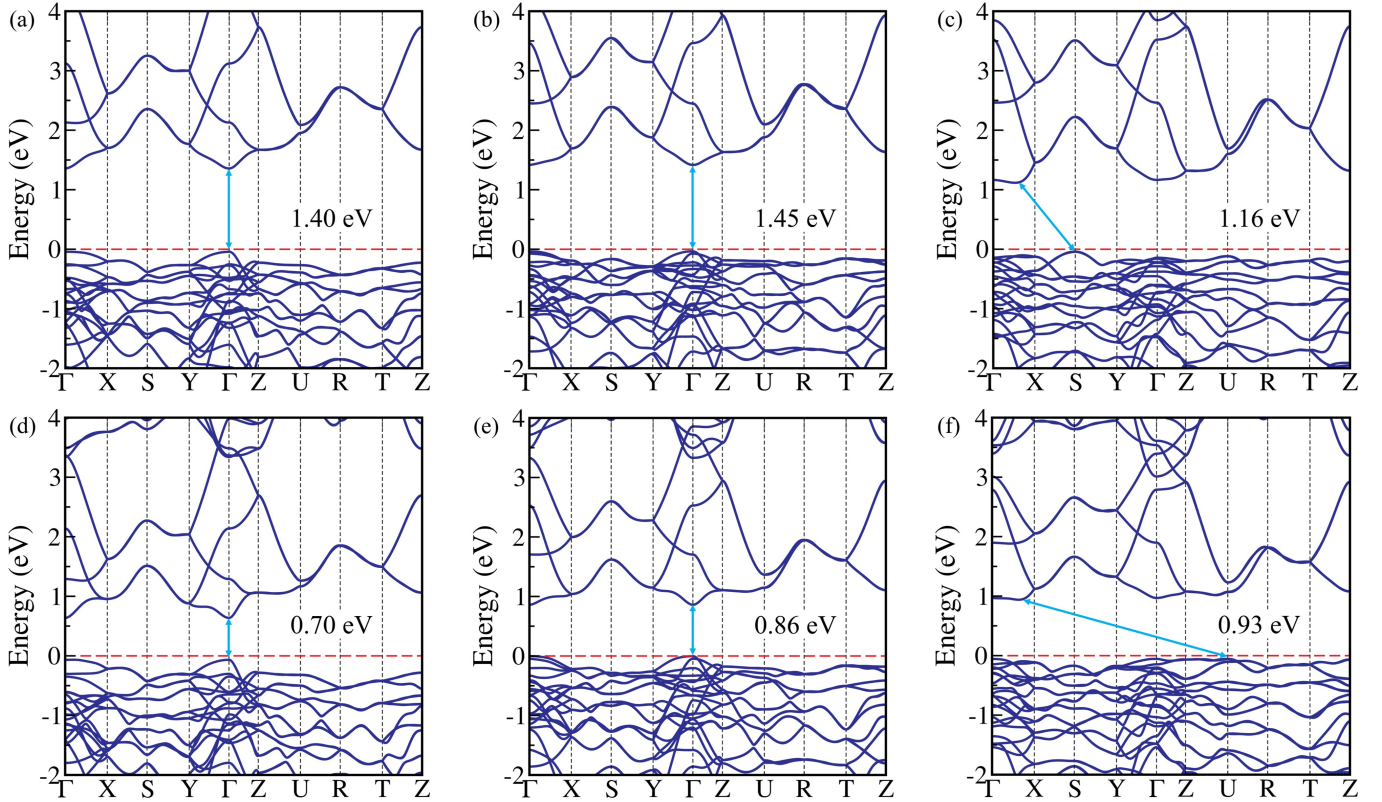


Figure 2. Electronic band structures of (a)  $\text{CaSnS}_3$ , (b)  $\text{SrSnS}_3$ , (c)  $\text{BaSnS}_3$ , (d)  $\text{CaSnSe}_3$ , (e)  $\text{SrSnSe}_3$ , and (f)  $\text{BaSnSe}_3$  chalcogenide perovskites, obtained using the HSE06 xc functional. The Fermi level is set to be zero and marked by the dashed line.

Figure S2 shows the partial density of states (PDOS) and the total density of states (TDOS) for all the studied compounds obtained using the HSE06 xc functional. In  $\text{ASnS}_3$  ( $A = \text{Ca}, \text{Sr}, \text{Ba}$ ) CPs, S-3*p* orbitals mostly contribute to the VBM, while the hybridization of S-3*p* and Sn-5*s* orbitals dominates the CBM. Similarly, for  $\text{ASnSe}_3$  perovskites, the VBM is primarily contributed by Se-4*p* orbitals, whereas CBM mainly consists of hybridized Se-4*p* and Sn-5*s* orbitals. The hybridization of Se-4*p* and Sn-5*s* orbitals in  $\text{ASnSe}_3$  is stronger than the hybridization of S-3*p* and Sn-5*s* orbitals in  $\text{ASnS}_3$ , which is mainly responsible for lowering the bandgap in case of  $\text{ASnSe}_3$  as compared to their sulfur counterparts  $\text{ASnS}_3$ .

Notably, perovskites are highly recognized for their ability to transport materials. Therefore, in addition to their band structures, we also calculate the corresponding electron ( $m_e^*$ ) and hole ( $m_h^*$ ) effective masses by utilizing the fitted E–k dispersion band diagram of  $G_0W_0$ @PBE band structures (Figure S3), employing the formula,  $m^* = \hbar^2 [\partial^2 E(k)/\partial k^2]^{-1}$  (for details, see the SM). From Table III, it is observed that  $m_e^* < 1$ ,  $m_h^* < 1.5$  for all the cases, indicating high carrier mobility and thus better charge carrier transport. Since  $\text{BaSnX}_3$  ( $X = \text{S}, \text{Se}$ ) exhibits an indirect bandgap, the effective masses for these compounds are calculated at both of their indirect and direct band edges. Also, Table III suggests that Ca- and Sr-based CPs have a high potential for exhibiting ambipolar characteristics.

Table III. Effective mass of electron ( $m_e^*$ ) and hole ( $m_h^*$ ) and their reduced mass ( $\mu^*$ ), obtained using the  $G_0W_0$ @PBE method. All values are in terms of free-electron mass ( $m_0$ ) and the bold values provided in parentheses are the effective mass and respective reduced mass at direct band edge.

Configurations	$m_e^* (m_0)$	$m_h^* (m_0)$	$\mu^* (m_0)$
$\text{CaSnS}_3$	0.403	0.537	0.230
$\text{SrSnS}_3$	0.608	0.673	0.319
$\text{BaSnS}_3$	0.674 ( <b>0.674</b> )	1.287 ( <b>1.121</b> )	0.442 ( <b>0.421</b> )
$\text{CaSnSe}_3$	0.149	0.207	0.087
$\text{SrSnSe}_3$	0.240	0.385	0.148
$\text{BaSnSe}_3$	0.717 ( <b>0.717</b> )	1.059 ( <b>1.237</b> )	0.428 ( <b>0.454</b> )

### C. Optical Properties:

The above study shows that the electronic properties of these CPs can be well-described by the HSE06 functional. Nevertheless, this functional is known to predict the optical features of these systems with less accuracy. Thus, we performed MBPT-based GW-BSE calculations to calculate the optical properties. In essence, GW calculations compute the fundamental bandgap, which is thought to be more accurate and comparable to photoelectron spectroscopy (PES) and inverse photoelectron spectroscopy (IPES)[40, 41], while BSE calculations predict the optical bandgap similar to experimental optical absorption spectroscopy[42, 43].

To evaluate the optical responses of the  $\text{ASnX}_3$  CPs, BSE calculations are performed on top of the single-shot  $\text{GW}(\text{G}_0\text{W}_0)\text{@PBE}$ , which explicitly considers the electron-hole interaction. The real  $[\text{Re}(\epsilon_e)]$  and imaginary  $[\text{Im}(\epsilon_e)]$  part of the frequency-dependent electronic dielectric function calculated using  $\text{BSE@G}_0\text{W}_0\text{@PBE}$  are shown in Figure 3. It is discovered that the absorption onset and the first peak position ( $E_o$ ) gradually red shift from sulfide (S) to selenide (Se) containing CPs akin to the drop of quasiparticle (QP) bandgap of them (see Table II). For example, the first peak position for  $\text{CaSnS}_3$  is observed at 1.23 eV, and it shifts to 0.74 eV for  $\text{CaSnSe}_3$ . The value of  $E_o$  for these  $\text{ASnX}_3$  CPs falls within the range of 0.74 to 1.26 eV and shifts with the change of the A atom, similar to the variation observed in their QP bandgap (see Table IV). The electronic dielectric constants ( $\epsilon_\infty$ ), which are obtained from the real part of the dielectric function, also found to be increased from S to Se containing CPs indicating low charge carrier recombination rate and improved optoelectronic efficiency for the latter[70] (see Table IV). For instance,  $\epsilon_\infty$  for  $\text{CaSnS}_3$  is 7.47, and it increases to 15.15 for  $\text{CaSnSe}_3$ . Overall, these results reveal that  $\text{CaSnS}_3$ ,  $\text{SrSnS}_3$ ,  $\text{BaSnS}_3$ , and  $\text{BaSnSe}_3$  could be the best choice for photovoltaic applications.

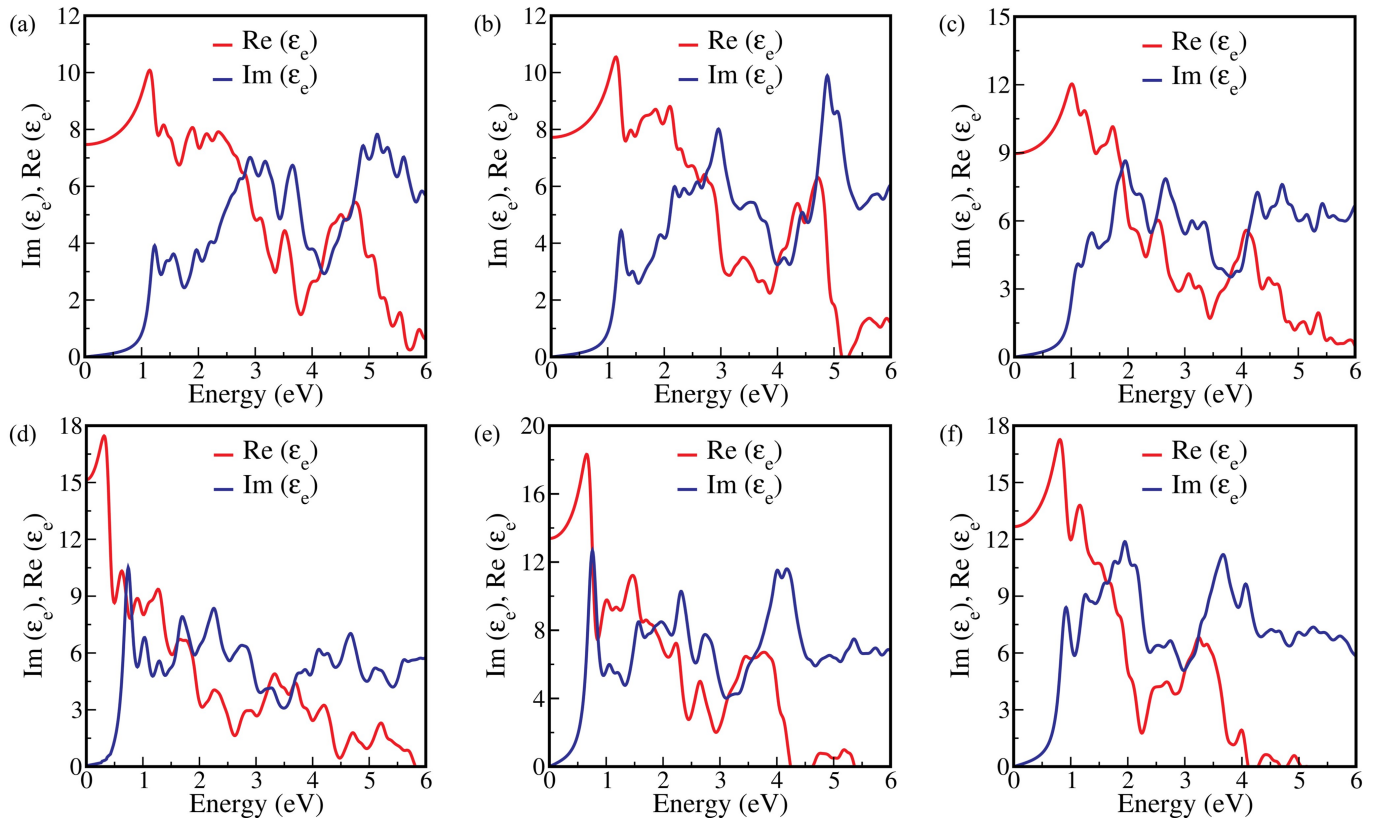


Figure 3. Computed real  $[\text{Re}(\epsilon_e)]$  and imaginary  $[\text{Im}(\epsilon_e)]$  part of the electronic dielectric function for (a)  $\text{CaSnS}_3$ , (b)  $\text{SrSnS}_3$ , (c)  $\text{BaSnS}_3$ , (d)  $\text{CaSnSe}_3$ , (e)  $\text{SrSnSe}_3$ , and (f)  $\text{BaSnSe}_3$  chalcogenide perovskites, obtained using the  $\text{BSE@G}_0\text{W}_0\text{@PBE}$  method.

The absorption coefficient  $[\alpha(\omega)]$  of a material is a measurable parameter that indicates how many photons (of a specific wavelength) may enter the material before being absorbed. Thus, this descriptor is also essential for photovoltaic applications and offers crucial information regarding the ideal solar energy conversion efficiency.  $\alpha(\omega)$  is

associated with the dielectric function and can be computed with the following formula[35]:

$$\alpha(\omega) = \sqrt{2}\omega \left[ \sqrt{(Re(\varepsilon_e))^2 + (Im(\varepsilon_e))^2} - Re(\varepsilon_e) \right]^{1/2}. \quad (13)$$

Our results from the BSE@G<sub>0</sub>W<sub>0</sub>@PBE calculation (see Figure S4) imply that all the investigated ASnX<sub>3</sub> CPs exhibit high optical absorption coefficients ( $\sim 10^4 - 10^5 \text{ cm}^{-1}$ ), which is desirable for the photovoltaic applications.

#### D. Excitonic Properties:

In optoelectronic materials, exciton generation plays a major role in the charge separation properties and for this reason, excitonic parameters, such as exciton binding energy ( $E_B$ ) and exciton lifetime ( $\tau_{exc}$ ), are crucial descriptors in their applications. The energy required to dissociate an exciton into a single electron ( $e$ ) and hole ( $h$ ) pair is known as the exciton binding energy. Theoretically,  $E_B$  is computed as the difference of the QP band gap (direct G<sub>0</sub>W<sub>0</sub>@PBE bandgap,  $E_g^d$ ) and the optical band gap (BSE@G<sub>0</sub>W<sub>0</sub>@PBE peak position,  $E_o$ )[56, 71–73], which are tabulated in Table IV. It should be noted that the electronic contribution of the dielectric screening is dominant over the ionic one if  $E_B$  is significantly greater than the longitudinal optical phonon energy ( $\hbar\omega_{LO}$ ). In that scenario, one can neglect the ionic contribution and consequently,  $E_B$  remains unchanged[74, 75]. From Table IV and Table VI, it is found that  $E_B \gg \hbar\omega_{LO}$  for ASnX<sub>3</sub> CPs; therefore, ionic screening to the dielectric function can be disregarded. The  $E_B$  values obtained from standard first-principles GW-BSE calculations are found in the range of 0.05–0.24 eV, which are comparable to that of Zr- and Hf-based CPs (0.02–0.26 eV)[14, 15, 22] but a little higher than those observed in conventional lead-based HPs (0.01–0.10 eV)[23–25] (for details, see Table S13 of the SM), which ensure the potential of these materials for the optoelectronic applications. Here, CaSnSe<sub>3</sub> exhibits the lowest  $E_B$  value, attributed to its higher electronic dielectric constant ( $\varepsilon_\infty$ ), which reduces the Coulomb interaction between the electron and hole.

Table IV. Excitonic parameters for chalcogenide perovskites.

Configurations	First-principles method (GW-BSE)						Wannier–Mott model			
	$E_g^d$ (eV)	$E_o$ (eV)	$E_B$ (eV)	$T_{exc}$ (K)	$r_{exc}$ (nm)	$ \phi_n(0) ^2$ ( $10^{26}m^{-3}$ )	$\varepsilon_\infty$	$E_{Bu}$ (meV)	$\varepsilon_{static}$	$E_{Bl}$ (meV)
CaSnS <sub>3</sub>	1.44	1.23	0.21	2435	1.72	0.63	7.47	56.06	34.70	2.60
SrSnS <sub>3</sub>	1.50	1.26	0.24	2783	1.28	1.52	7.72	72.79	32.55	4.09
BaSnS <sub>3</sub>	1.28	1.12	0.16	1855	1.13	2.21	8.97	71.16	45.61	2.75
CaSnSe <sub>3</sub>	0.79	0.74	0.05	580	9.21	0.004	15.15	5.16	70.08	0.24
SrSnSe <sub>3</sub>	0.88	0.78	0.10	1159	4.79	0.03	13.39	11.23	56.98	0.62
BaSnSe <sub>3</sub>	1.04	0.91	0.13	1507	1.48	0.99	12.67	38.46	44.66	3.10

In addition, we have validated the  $E_B$  using the Wannier-Mott method[22, 56] through the Eq. 1. Here,  $\varepsilon_{eff}$  lies in between optical ( $\varepsilon_\infty$ ) and static ( $\varepsilon_{static}$ ) dielectric constant. The optical or electronic dielectric constants ( $\varepsilon_\infty$ ) at the zero frequency limit are obtained using BSE method. Subsequently, the DFPT calculations are performed to compute the ionic contribution to the dielectric function ( $\varepsilon_{ion}$ ), and therefore, the static dielectric constant is calculated as,  $\varepsilon_{static} = (\varepsilon_\infty + \varepsilon_{ion})$ . In our study, the upper ( $E_{Bu}$ ) and lower ( $E_{Bl}$ ) bounds of exciton binding energy are estimated based on the  $\varepsilon_\infty$  and  $\varepsilon_{static}$ , respectively (see Table IV). The upper bound values are smaller but align more closely with the  $E_B$  calculated using the GW-BSE method compared to the lower bound values; however, the overall trend remains consistent. This suggests that in chalcogenide perovskites, the electronic contribution to dielectric screening is more prominent than the ionic contribution.

Furthermore, additional investigations into the ionic (phonon) contribution to the exciton binding energy ( $E_B$ ) are conducted for the examined CPs. This is because the standard BSE approach within an ab-initio framework captures only static screening from electrons to calculate the exciton binding energy. However, it's noteworthy that dynamic electron-electron interactions or electron-phonon coupling may play a crucial role in certain materials, particularly those with significant electron-phonon interactions or where phonons significantly influence optoelectronic properties. Filip and collaborators[57] have recently broadened the discussion to incorporate phonon screening into the analysis of exciton binding energy using equation 2. They achieved this by considering four specific material parameters: reduced effective mass, static and optical dielectric constants, and the frequency of the longitudinal optical phonon mode ( $\omega_{LO}$ ), while assuming isotropic and parabolic electronic band dispersion. Table V indicates that phonon screening leads to a reduction in the  $E_B$  ranging from 5.58% to 17.87%, with the modified  $E_B$  values ranging from 0.04 to 0.23 eV. While phonon screening does decrease the exciton binding energy, the reduction is not particularly substantial, except in the case of CaSnSe<sub>3</sub>. This also suggests that in the majority of chalcogenide perovskites, the electronic contribution to dielectric screening outweighs the ionic (or phonon) contribution.

Table V. Calculated exciton binding energy ( $E_B$ ), phonon screening corrections ( $\Delta E_B^{ph}$ ), percentage of phonon screening contribution to the reduction of exciton binding energy (%), and corrected values of exciton binding energy ( $E_B + \Delta E_B^{ph}$ ) for chalcogenide perovskites.

Configurations	$E_B$ (meV)	$\Delta E_B^{ph}$ (meV)	Reduction of $E_B$ (%)	$(E_B + \Delta E_B^{ph})$ (meV)
CaSnS <sub>3</sub>	210	-14.68	6.99	195.32
SrSnS <sub>3</sub>	240	-13.39	5.58	226.61
BaSnS <sub>3</sub>	160	-12.42	7.76	147.58
CaSnSe <sub>3</sub>	50	-8.93	17.87	41.07
SrSnSe <sub>3</sub>	100	-8.17	8.17	91.83
BaSnSe <sub>3</sub>	130	-8.08	6.22	121.92

Several excitonic parameters, including excitonic temperature ( $T_{exc}$ ), exciton radius ( $r_{exc}$ ), and probability of wave function ( $|\phi_n(0)|^2$ ) for  $e-h$  pair at zero charge separation are also computed using the above quantities ( $E_B$ ,  $\varepsilon_\infty$ , and  $\mu^*$ ) to have a definitive estimation of the excitonic properties (for details, see the SM). The inverse of  $|\phi_n(0)|^2$  can be used to qualitatively characterize the exciton lifetime ( $\tau_{exc}$ ), which is listed in Table IV (for details, see the SM). Consequently, the  $\tau_{exc}$  values for the investigated CPs are in the order CaSnSe<sub>3</sub> > SrSnSe<sub>3</sub> > CaSnS<sub>3</sub> > BaSnSe<sub>3</sub> > SrSnS<sub>3</sub> > BaSnS<sub>3</sub>. A longer exciton lifetime corresponds to a lower carrier recombination rate, which enhances the quantum yield and conversion efficiency. Overall, these properties significantly enhance the efficiency of ASnX<sub>3</sub> CPs, making them promising for potential optoelectronic applications.

### E. Polaronic Properties:

In polar semiconductors, such as halide perovskite and its derivatives, the scattering mechanism near room temperature is dominant due to the interaction between charge carriers and the macroscopic electric field produced by longitudinal optical phonon (LO)[59]. This interaction strongly influences charge carrier mobility of the system and is anticipated to be same for the materials of our interest[14, 22]. Therefore, the Fröhlich mesoscopic model[26, 59, 76] is used to describe this interaction and defined by the dimensionless Fröhlich parameter  $\alpha$  using Eq. 3. The calculated values of  $\alpha$  related to Fröhlich interaction for electrons and holes are given in Table VI and Table S11, respectively. Strong electron (hole)-phonon coupling is indicated by  $\alpha > 10$ , while  $\alpha \ll 1$  often suggests weak coupling[26]. Our results show that the value of  $\alpha$  for ASnX<sub>3</sub> CPs lies in the range of 0.64–2.92, suggesting weak to intermediate electron (hole)-phonon coupling for the investigated systems. Here, CaSnSe<sub>3</sub> exhibits smaller electron-phonon coupling, while BaSnS<sub>3</sub> demonstrates larger electron-phonon coupling. Weak electron-phonon coupling can be attributed to factors such as a lower electron effective mass and a higher electronic dielectric constant. Conversely, strong coupling arises from the opposite factors. In this context, the specific free volume of these CPs are also evaluated to obtain a qualitative knowledge of the strength of electron-phonon coupling (for details, see the SM).

Notably, polaron formation can lead to a decrease in the electron and hole QP energies. This polaron energy ( $E_p$ ) can also be calculated using  $\alpha$  by using Eq. 4. The QP gap, which results from the polaron energy for electrons and holes, is reduced by 76.37, 81.16, 85.32, 18.58, 25.37, and 43.65 meV for CaSnS<sub>3</sub>, SrSnS<sub>3</sub>, BaSnS<sub>3</sub>, CaSnSe<sub>3</sub>, SrSnSe<sub>3</sub>, and BaSnSe<sub>3</sub>, respectively. Comparing the values of  $E_B$  from Table IV with the QP gap, it is evident that the energy of charge-separated polaronic states is lower than that of the bound exciton states. This suggests that the charge-separated polaronic states are less stable than the bound excitons.

The other parameters for the polarons, i.e., polaron mass ( $m_p$ ) and polaron mobility ( $\mu_p$ ), are also estimated using Eq. 5 and Eq. 6, respectively. These parameter values are listed in Table VI and Table S11 for electrons and holes, respectively. One can confirm the enhanced carrier-lattice interactions by higher  $m_p$  values, and for this case, the charge carrier mobility decreases than the non-polar or less polar compounds. For example, Ca- and Sr-based compounds exhibit weaker carrier (electron)-lattice interactions compared to Ba-based compounds, resulting in higher mobility for Ca- and Sr-based materials. Also, CaSnSe<sub>3</sub> CP exhibit highest polaron mobility for electron which is obvious due to weak electron-phonon coupling ( $\alpha = 0.64$ ). Overall, These Sn-based materials are shown to have ambipolar properties and much improved polaron mobility for electrons (21.33–416.02 cm<sup>2</sup>V<sup>-1</sup>s<sup>-1</sup>) and holes (7.02–260.69 cm<sup>2</sup>V<sup>-1</sup>s<sup>-1</sup>, see Table S11 of the SM) than the conventional lead-based HPs (57–290 cm<sup>2</sup>V<sup>-1</sup>s<sup>-1</sup> for electrons and 97–230 cm<sup>2</sup>V<sup>-1</sup>s<sup>-1</sup> for holes, respectively)[26, 27] as well as Zr- and Hf-based CPs (6.84–77.59 cm<sup>2</sup>V<sup>-1</sup>s<sup>-1</sup> for electrons and 3.76–100.49 cm<sup>2</sup>V<sup>-1</sup>s<sup>-1</sup> for holes, respectively)[14, 15, 22].



Table VI. Polaron parameters for electrons in chalcogenide perovskites.

Configurations	$\omega_{LO}$ (THz)	$\theta_D$ (K)	$\alpha$	$E_p$ (meV)	$m_p/m^*$	$\mu_p$ ( $\text{cm}^2\text{V}^{-1}\text{s}^{-1}$ )
CaSnS <sub>3</sub>	4.78	229.51	1.75	35.39	1.37	42.29
SrSnS <sub>3</sub>	4.44	213.18	2.10	39.61	1.46	22.64
BaSnS <sub>3</sub>	3.97	190.62	2.11	35.59	1.46	21.33
CaSnSe <sub>3</sub>	3.20	153.65	0.64	8.55	1.12	416.02
SrSnSe <sub>3</sub>	2.76	132.52	0.97	11.22	1.18	173.92
BaSnSe <sub>3</sub>	2.88	138.28	1.62	19.71	1.33	32.86

### F. Spectroscopic Limited Maximum Efficiency:

The above discussed properties indicate that the investigated systems hold great potential for photovoltaic applications and to validate this, we also calculated their power conversion efficiency (PCE). The theoretical PCE of each system is calculated using the spectroscopic limited maximum efficiency (SLME) method. SLME was introduced by Yu and Zunger[44] (for details, see the SM), which is an improved version of the Shockley-Queisser (SQ) limit[77]. The latter is less realistic since it disregards the losses resulting from radiative recombinations due to the non-conservation of the absorbed photon momentum. SLME incorporates the magnitude of the bandgap and its nature (direct or indirect), shape of absorption spectra, thickness of the absorber layer, the material-dependent non-radiative recombination losses, and the temperature. The standard solar spectrum (AM-1.5G), the absorption coefficient, thickness, and the electronic  $G_0W_0$ @PBE bandgap are thus used as inputs to evaluate the theoretical SLME of  $\text{ASnX}_3$  ( $A = \text{Ca, Sr, Ba}$ ;  $X = \text{S, Se}$ ) CPs at 293.15 K temperature.

In addition, the optical transition possibility from VBM to CBM for these CPs has been confirmed through the computation of transition dipole moment matrix (P) elements; its square ( $P^2$ ) gives the transition probability between the initial (VBM) and the final (CBM) state. Figure 4(a) shows the optically allowed dipole transition at  $\Gamma$ -point for CaSnS<sub>3</sub>, and for other configurations, see Figure S5. Despite having an indirect electronic bandgap, BaSnS<sub>3</sub> and BaSnSe<sub>3</sub> exhibit an optically allowed dipole transition at their direct band edge. However, when  $E_g^{da}$  is not the minimum bandgap of the materials (i.e.,  $E_g \neq E_g^{da}$ ), non-radiative recombination plays a vital role in the SLME calculation and the radiative recombinations vary with a factor  $f_r = e^{-\Delta/k_B T}$ , where  $\Delta = E_g^{da} - E_g$ ,  $k_B$  is the Boltzmann constant, and T is the temperature[44] (for details, see the SM).

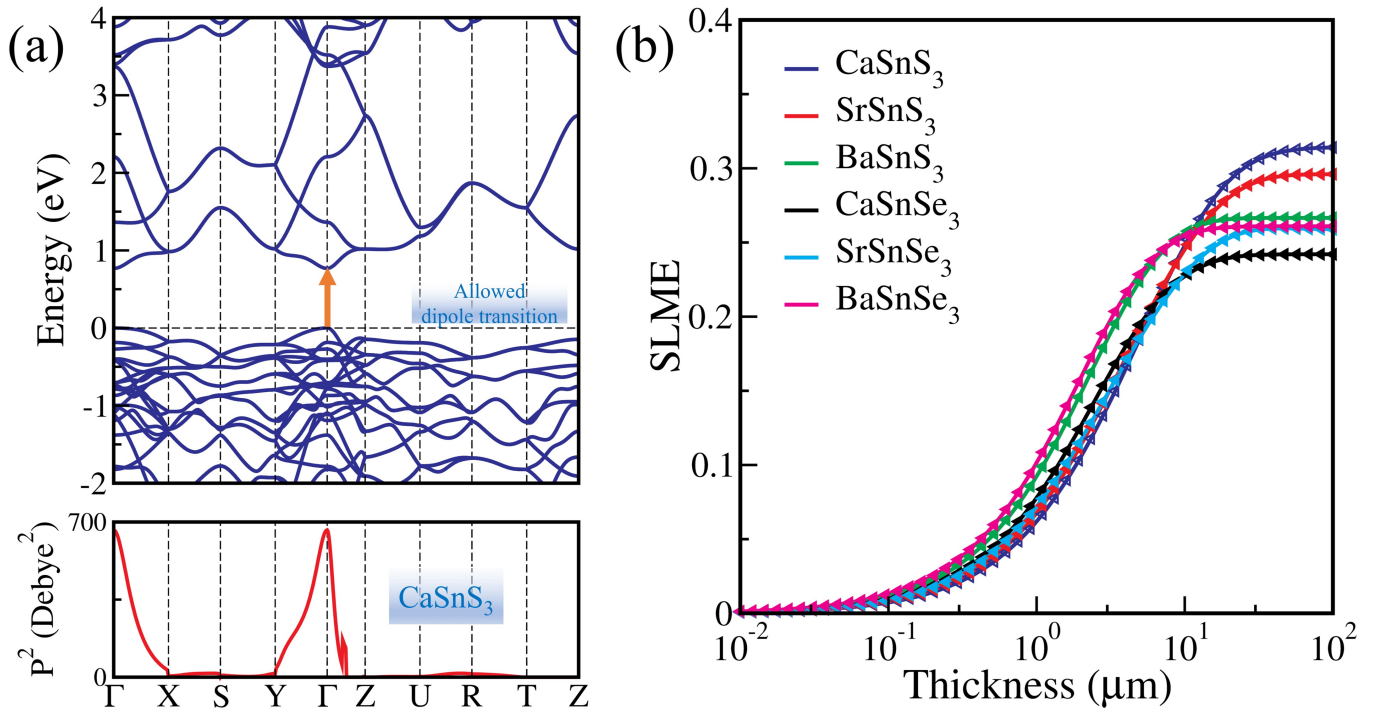


Figure 4. (a) Electronic band structure and transition probability (square of the transition dipole moment matrix elements) of  $\text{CaSnS}_3$  calculated using PBE, and (b) spectroscopic limited maximum efficiency (SLME) of  $\text{ASnX}_3$  ( $A = \text{Ca}, \text{Sr}, \text{Ba}$ ;  $X = \text{S}, \text{Se}$ ) chalcogenide perovskites calculated using BSE@ $G_0W_0$ @PBE method.

Next, the thickness dependence of SLME has been computed for all the  $\text{ASnX}_3$  ( $A = \text{Ca}, \text{Sr}, \text{Ba}$ ;  $X = \text{S}, \text{Se}$ ) compounds using BSE@ $G_0W_0$ @PBE method and plotted in Figure 4(b). It is clear that the SLME rises as thickness increases and eventually saturates beyond a certain thickness. The maximum SLME is found to be 31.20% for  $\text{CaSnS}_3$ , which is consistent with the previously documented theoretical efficiency of 32.45% at 10  $\mu\text{m}$  thickness[14] and is higher than  $\text{CH}_3\text{NH}_3\text{PbI}_3$  (28.97% at 2  $\mu\text{m}$ )[28]. The highest SLME values for  $\text{SrSnS}_3$ ,  $\text{BaSnS}_3$ ,  $\text{CaSnSe}_3$ ,  $\text{SrSnSe}_3$ , and  $\text{BaSnSe}_3$  compounds are calculated as 29.53%, 26.66%, 24.20%, 25.95%, and 26.09%, respectively. These values of SLME are favorable for the photovoltaic applications compared to  $\text{ABS}_3$  ( $A = \text{Ca}, \text{Sr}, \text{Ba}$ ;  $B = \text{Zr}, \text{Hf}$ ),  $\text{CsGeX}_3$  ( $X = \text{Cl}, \text{Br}, \text{I}$ ), and other halide perovskites[14, 22, 78–80] (for details, see Table S13 of the SM).



## G. Analysis of SCAPS-1D results:

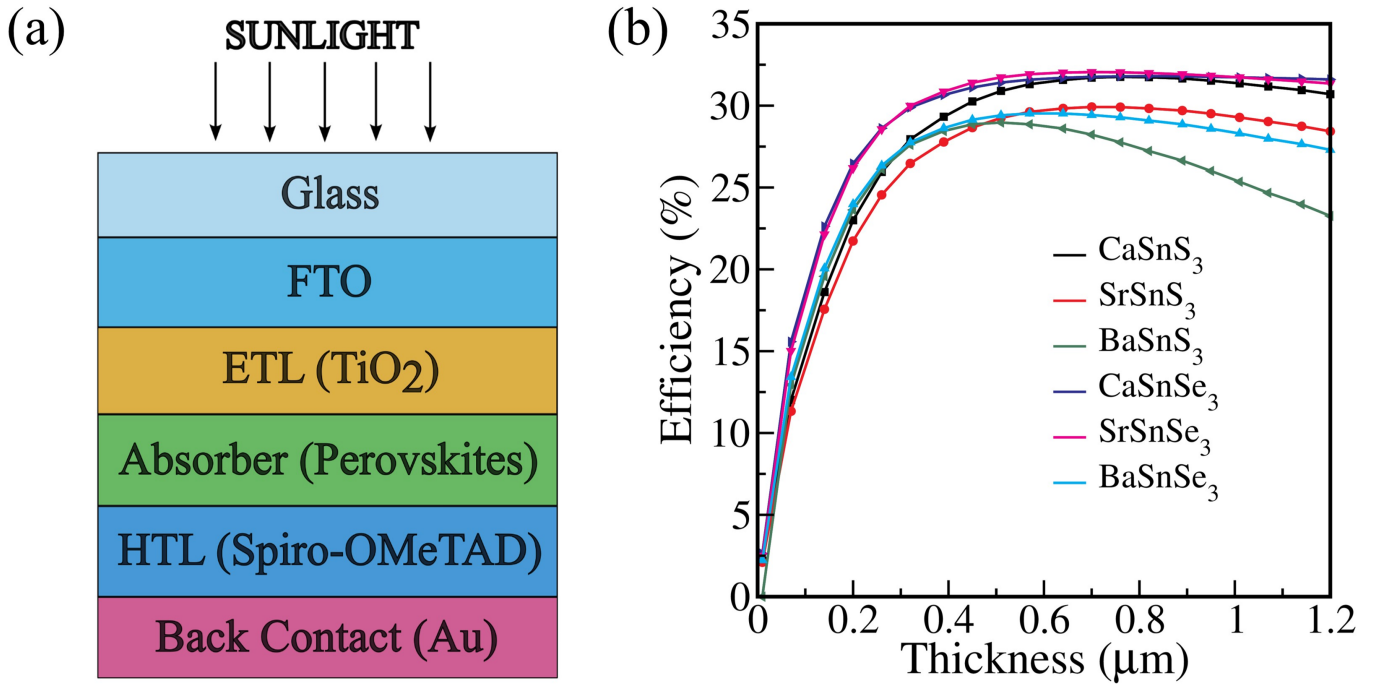


Figure 5. (a) Schematic of the simulated device structure and (b) power conversion efficiency (PCE) of the  $ASnX_3$  ( $A = Ca, Sr, Ba; X = S, Se$ ) chalcogenide perovskites-based PSC using SCAPS-1D.

To verify the photovoltaic potential of the investigated systems and our calculated SLME, we also conducted a detailed analysis using the Solar Cell Capacitance Simulator in 1 Dimension (SCAPS-1D). This simulation allowed us to evaluate key performance metrics and gain deeper insights into the efficiency and operational behavior of the devices. Here, the performance of PSC is evaluated by varying the thickness of the absorber layer while keeping the ETL, HTL, and FTO thicknesses constant. The absorber layer thickness is varied from  $0.01 \mu\text{m}$  to  $1.2 \mu\text{m}$  and found that the thickness of the perovskite layer has a significant impact on the performance of the PSC [see Figure 5(b)]. After reaching the optimum efficiency, the effect of the thickness of the perovskite layer seems to saturate, in agreement to our SLME calculations. The obtained results are summarized in the Table VII. Our findings indicate that the device simulation results are consistent with the SLME work, specifically for  $ASnS_3$  ( $A = Ca, Sr, Ba$ ). On the other hand, the minor discrepancies between the device simulation results for  $ASnSe_3$  ( $A = Ca, Sr, Ba$ ) and the SLME findings may be attributed to the materials used in the ETL, HTL, and FTO layers. In general, SCAPS-1D proves to be a highly reliable software, as its simulation results confirm the high efficiency of the investigated materials, closely aligning with theoretical predictions.

Table VII. Photovoltaic parameters of  $ASnX_3$  ( $A = Ca, Sr, Ba; X = S, Se$ ) chalcogenide perovskites based solar cells using SCAPS-1D.

Optimized Device	$V_{oc}$ (V)	$J_{sc}$ (mA/cm <sup>2</sup> )	FF (%)	PCE (%)
FTO/TiO <sub>2</sub> /CaSnS <sub>3</sub> /Spiro-OMeTAD/Au	1.2885	27.49796	89.63	31.76
FTO/TiO <sub>2</sub> /SrSnS <sub>3</sub> /Spiro-OMeTAD/Au	1.3239	25.06713	90.15	29.92
FTO/TiO <sub>2</sub> /BaSnS <sub>3</sub> /Spiro-OMeTAD/Au	0.9871	33.93041	86.49	28.97
FTO/TiO <sub>2</sub> /CaSnSe <sub>3</sub> /Spiro-OMeTAD/Au	0.7255	55.85582	82.92	31.80
FTO/TiO <sub>2</sub> /SrSnSe <sub>3</sub> /Spiro-OMeTAD/Au	0.7750	49.34989	83.80	32.05
FTO/TiO <sub>2</sub> /BaSnSe <sub>3</sub> /Spiro-OMeTAD/Au	0.8050	43.53916	84.22	29.52

Overall, study of all the above discussed properties collectively show that Se-based  $CaSnSe_3$  and  $SrSnSe_3$  demonstrate lower exciton binding energies and higher charge carrier mobilities than the rest of the investigated systems. However, their SLME is also relatively low. On the other hand, S-based  $CaSnS_3$  and  $SrSnS_3$  perovskites exhibit higher SLME despite having higher exciton binding energies and lower charge carrier mobilities compared to the other ex-

aminated materials. This improved SLME is primarily attributed to the optimal bandgaps of  $\text{CaSnS}_3$  and  $\text{SrSnS}_3$  compared to their selenium (Se) counterparts, specifically from the perspective of solar cells. This reveals a trade-off between exciton binding energy and charge carrier mobility, and the bandgap of these materials. This suggests that integrating a combination of sulfur (S) and selenium (Se) atoms in these materials could be advantageous for potential application in solar cells, meriting further investigation.

#### IV. CONCLUSIONS:

In conclusion, we have carried out a comprehensive study to investigate the ground- and excited-state properties of distorted chalcogenide perovskites ( $\text{ASnX}_3$ ; A = Ca, Sr, Ba, and X = S, Se) under the framework of state-of-the-art DFT combined with DFPT and MBPT (viz., GW and BSE). The mechanical properties confirm the stability, and Pugh's and Poisson's ratios reveal the ductile nature of these perovskites. The bandgaps calculated using  $G_0W_0@PBE$  method are in the range of 0.79–1.50 eV, and the small effective masses of electrons suggest good charge carrier mobility, which is advantageous for energy-harvesting properties. Furthermore, they have a high optical absorption coefficient ( $> 10^4 \text{ cm}^{-1}$ ) and an optical bandgap extending from the near-infrared to the visible range, which are indicated by the BSE calculations. The exciton binding energies of these compounds, ranging from 0.04 to 0.23 eV, are similar to those of Zr- and Hf-based CPs but are little higher than those typically found in conventional lead-based HPs. Also, these perovskites have smaller carrier-phonon coupling strengths than the conventional lead-based HPs as well as Zr- and Hf-based CPs, which leads to better polaron mobility for electrons ( $21.33\text{--}416.02 \text{ cm}^2\text{V}^{-1}\text{s}^{-1}$ ) and holes ( $7.02\text{--}260.69 \text{ cm}^2\text{V}^{-1}\text{s}^{-1}$ ). Additionally, the Fröhlich mesoscopic model implies that the charge-separated polaronic states have lower stability in comparison to bound excitons. Lastly, the SLME method forecasts that one could achieve the highest PCE of up to 31.20% by employing them, which is corroborated by conventional device (FTO/ $\text{TiO}_2$ / $\text{ASnX}_3$ /Spiro-OMeTAD/Au) simulations using SCAPS-1D software. Overall, these results are anticipated to expedite the research and use of chalcogenide perovskites in optoelectronic applications, in general, and solar cell technology, in particular.

#### ACKNOWLEDGMENTS

The authors would like to acknowledge the Council of Scientific and Industrial Research (CSIR), Government of India [Grant No. 3WS(007)/2023-24/EMR-II/ASPIRE] for financial support. S.A. would also like to acknowledge the CSIR, India [Grant No. 09/1128(11453)/2021-EMR-I] for the Senior Research Fellowship. S. D. thanks Prof. Marc Burgelman, Department of Electronics and Information Systems (ELIS), University of Gent, for providing the SCAPS-1D software. The high performance computing facility "Magus" and workstations available at the School of Natural Sciences, Shiv Nadar Institution of Eminence (SNIoE), were used to perform all calculations.

- 
- [1] D. Tiwari, O. S. Hutter, and G. Longo, *J. Phys. Energy* **3**, 034010 (2021).
  - [2] S. Niu, H. Huyan, Y. Liu, M. Yeung, K. Ye, L. Blankemeier, T. Orvis, D. Sarkar, D. J. Singh, R. Kapadia, and J. Ravichandran, *Adv. Mater.* **29**, 1604733 (2017), <https://onlinelibrary.wiley.com/doi/pdf/10.1002/adma.201604733>.
  - [3] X. Wu, W. Gao, J. Chai, C. Ming, M. Chen, H. Zeng, P. Zhang, S. Zhang, and Y.-Y. Sun, *Sci. China Mater.* **64**, 2976 (2021).
  - [4] Y.-Y. Sun, M. L. Agiorgousis, P. Zhang, and S. Zhang, *Nano Lett.* **15**, 581 (2015), <https://doi.org/10.1021/nl504046x>.
  - [5] A. Kojima, K. Teshima, Y. Shirai, and T. Miyasaka, *J. Am. Chem. Soc.* **131**, 6050 (2009), <https://doi.org/10.1021/ja809598r>.
  - [6] N.-G. Park, *J. Phys. Chem. Lett.* **4**, 2423 (2013), <https://doi.org/10.1021/jz400892a>.
  - [7] J. Berry, T. Buonassisi, D. A. Egger, G. Hodes, L. Kronik, Y.-L. Loo, I. Lubomirsky, S. R. Marder, Y. Mastai, J. S. Miller, D. B. Mitzi, Y. Paz, A. M. Rappe, I. Riess, B. Rybtchinski, O. Stafsudd, V. Stevanovic, M. F. Toney, D. Zitoun, A. Kahn, D. Ginley, and D. Cahen, *Adv. Mater.* **27**, 5102 (2015), <https://onlinelibrary.wiley.com/doi/pdf/10.1002/adma.201502294>.
  - [8] D. A. Egger, A. M. Rappe, and L. Kronik, *Acc. Chem. Res.* **49**, 573 (2016), <https://doi.org/10.1021/acs.accounts.5b00540>.
  - [9] D. B. Straus, S. Guo, A. M. Abeykoon, and R. J. Cava, *Adv. Mater.* **32**, 2001069 (2020), <https://onlinelibrary.wiley.com/doi/pdf/10.1002/adma.202001069>.
  - [10] A. Babayigit, A. Ethirajan, M. Muller, and B. Conings, *Nat. Mater.* **15**, 247 (2016).
  - [11] A. Swarnkar, W. J. Mir, R. Chakraborty, M. Jagadeeswararao, T. Sheikh, and A. Nag, *Chem. Mater.* **31**, 565 (2019), <https://doi.org/10.1021/acs.chemmater.8b04178>.
  - [12] K. V. Sopiha, C. Comparotto, J. A. Marquez, and J. J. S. Scragg, *Adv. Optical Mater.* **10**, 2101704 (2022), <https://onlinelibrary.wiley.com/doi/pdf/10.1002/adom.202101704>.

- [13] K. Kuhar, A. Crovetto, M. Pandey, K. S. Thygesen, B. Seger, P. C. K. Vesborg, O. Hansen, I. Chorkendorff, and K. W. Jacobsen, *Energy Environ. Sci.* **10**, 2579 (2017).
- [14] P. Basera and S. Bhattacharya, *J. Phys. Chem. Lett.* **13**, 6439 (2022), <https://doi.org/10.1021/acs.jpcclett.2c01337>.
- [15] S. Adhikari and P. Johari, *Phys. Rev. B* **109**, 174114 (2024).
- [16] D. Liu, H. Zeng, H. Peng, and R. Sa, *Phys. Chem. Chem. Phys.* **25**, 13755 (2023).
- [17] R. Lelieveld and D. J. W. IJdo, *Acta Cryst. B* **36**, 2223 (1980).
- [18] C.-S. Lee, K. Kleinke, and H. Kleinke, *Solid State Sci.* **7**, 1049 (2005).
- [19] N. A. Moroz, C. Bauer, L. Williams, A. Olvera, J. Casamento, A. A. Page, T. P. Bailey, A. Weiland, S. S. Stoyko, E. Kioupakis, C. Uher, J. A. Aitken, and P. F. P. Poudeu, *Inorg. Chem.* **57**, 7402 (2018), <https://doi.org/10.1021/acs.inorgchem.8b01038>.
- [20] L. J. Tranchitella, B.-H. Chen, J. C. Fettinger, and B. W. Eichhorn, *J. Solid State Chem.* **130**, 20 (1997).
- [21] S. Perera, H. Hui, C. Zhao, H. Xue, F. Sun, C. Deng, N. Gross, C. Milleville, X. Xu, D. F. Watson, B. Weinstein, Y.-Y. Sun, S. Zhang, and H. Zeng, *Nano Energy* **22**, 129 (2016).
- [22] M. Kumar, A. Singh, D. Gill, and S. Bhattacharya, *J. Phys. Chem. Lett.* **12**, 5301 (2021).
- [23] H. M. Ghaithan, S. M. H. Qaid, Z. A. Alahmed, M. Hezam, A. Lyras, M. Amer, and A. S. Aldwayyan, *J. Phys. Chem. C* **125**, 886 (2021), <https://doi.org/10.1021/acs.jpcc.0c07983>.
- [24] R. Comin, G. Walters, E. S. Thibau, O. Voznyy, Z.-H. Lu, and E. H. Sargent, *J. Mater. Chem. C* **3**, 8839 (2015).
- [25] X. Chen, H. Lu, Y. Yang, and M. C. Beard, *J. Phys. Chem. Lett.* **9**, 2595 (2018), PMID: 29714488, <https://doi.org/10.1021/acs.jpcclett.8b00526>.
- [26] J. M. Frost, *Phys. Rev. B* **96**, 195202 (2017).
- [27] Y. Kang and S. Han, *Phys. Rev. Appl.* **10**, 044013 (2018).
- [28] Q. Sun, H. Chen, and W.-J. Yin, *Chem. Mater.* **31**, 244 (2019), <https://doi.org/10.1021/acs.chemmater.8b04320>.
- [29] H. Zou, Y. Duan, S. Yang, D. Xu, L. Yang, J. Cui, H. Zhou, M. Wu, J. Wang, X. Lei, N. Zhang, and Z. Liu, *Small* **19**, 2206205 (2023), <https://onlinelibrary.wiley.com/doi/pdf/10.1002/sml.202206205>.
- [30] R. Guo and S. Wang, *J. Phys. Chem. C* **123**, 29 (2019), <https://doi.org/10.1021/acs.jpcc.8b08041>.
- [31] M.-G. Ju, J. Dai, L. Ma, and X. C. Zeng, *Adv. Energy Mater.* **7**, 1700216 (2017), <https://onlinelibrary.wiley.com/doi/pdf/10.1002/aenm.201700216>.
- [32] H. Shaili, M. Beraich, A. El hat, M. Ouafi, E. mehdi Salmani, R. Essajai, W. Battal, M. Rouchdi, M. Taibi, N. Hassanain, and A. Mzerd, *J. Alloys Compd.* **851**, 156790 (2021).
- [33] P. Hohenberg and W. Kohn, *Phys. Rev.* **136**, B864 (1964).
- [34] W. Kohn and L. J. Sham, *Phys. Rev.* **140**, A1133 (1965).
- [35] M. Gajdoš, K. Hummer, G. Kresse, J. Furthmüller, and F. Bechstedt, *Phys. Rev. B* **73**, 045112 (2006).
- [36] H. Jiang, P. Rinke, and M. Scheffler, *Phys. Rev. B* **86**, 125115 (2012).
- [37] F. Fuchs, C. Rödl, A. Schleife, and F. Bechstedt, *Phys. Rev. B* **78**, 085103 (2008).
- [38] J. P. Perdew, K. Burke, and M. Ernzerhof, *Phys. Rev. Lett.* **77**, 3865 (1996).
- [39] J. Heyd, G. E. Scuseria, and M. Ernzerhof, *J. Chem. Phys.* **118**, 8207 (2003).
- [40] L. Hedin, *Phys. Rev.* **139**, A796 (1965).
- [41] M. S. Hybertsen and S. G. Louie, *Phys. Rev. Lett.* **55**, 1418 (1985).
- [42] S. Albrecht, L. Reining, R. Del Sole, and G. Onida, *Phys. Rev. Lett.* **80**, 4510 (1998).
- [43] M. Rohlffing and S. G. Louie, *Phys. Rev. Lett.* **81**, 2312 (1998).
- [44] L. Yu and A. Zunger, *Phys. Rev. Lett.* **108**, 068701 (2012).
- [45] A. Husainat, W. Ali, P. Cofie, J. Attia, and J. Fuller, *Am. J. Opt. Photonics* **7**, 33 (2019), <https://article.sciencepublishinggroup.com/pdf/10.11648.j.ajop.20190702.12>.
- [46] M. K. Hossain, A. A. Arnab, D. P. Samajdar, M. H. K. Rubel, M. M. Hossain, M. R. Islam, R. C. Das, H. Bencherif, M. F. Rahman, J. Madan, R. Pandey, S. Bhattarai, M. Amami, and D. K. Dwivedi, *Energy Fuels* **37**, 13377 (2023), <https://doi.org/10.1021/acs.energyfuels.3c02361>.
- [47] S. S. Nishat, M. J. Hossain, F. E. Mullick, A. Kabir, S. Chowdhury, S. Islam, and M. Hossain, *J. Phys. Chem. C* **125**, 13158 (2021), <https://doi.org/10.1021/acs.jpcc.1c02302>.
- [48] S. Ramawat, S. Kukreti, D. J. Sapkota, and A. Dixit, *Energy Fuels* **38**, 9011 (2024), <https://doi.org/10.1021/acs.energyfuels.4c00763>.
- [49] G. Kresse and J. Furthmüller, *Phys. Rev. B* **54**, 11169 (1996).
- [50] G. Kresse and J. Furthmüller, *Comput. Mater. Sci.* **6**, 15 (1996).
- [51] P. E. Blöchl, *Phys. Rev. B* **50**, 17953 (1994).
- [52] K. Momma and F. Izumi, *J. Appl. Crystallogr.* **44**, 1272 (2011).
- [53] A. Togo, L. Chaput, T. Tadano, and I. Tanaka, *J. Phys. Condens. Matter* **35**, 353001 (2023).
- [54] A. M. Ganose, A. J. Jackson, and D. O. Scanlon, *J. Open Source Softw.* **3**, 717 (2018).
- [55] V. Wang, N. Xu, J.-C. Liu, G. Tang, and W.-T. Geng, *Comput. Phys. Commun.* **267**, 108033 (2021).
- [56] S. Adhikari and P. Johari, *Phys. Rev. Mater.* **7**, 075401 (2023).
- [57] M. R. Filip, J. B. Haber, and J. B. Neaton, *Phys. Rev. Lett.* **127**, 067401 (2021).
- [58] R. W. Hellwarth and I. Biaggio, *Phys. Rev. B* **60**, 299 (1999).
- [59] M. Jain, P. Bhumla, M. Kumar, and S. Bhattacharya, *J. Phys. Chem. C* **126**, 6753 (2022), <https://doi.org/10.1021/acs.jpcc.2c00102>.
- [60] R. P. Feynman, *Phys. Rev.* **97**, 660 (1955).
- [61] M. Burgelman, P. Nollet, and S. Degraeve, *Thin Solid Films* **361-362**, 527 (2000).

- [62] M. Burgelman, K. Decock, S. Khelifi, and A. Abass, *Thin Solid Films* **535**, 296 (2013).
- [63] C. Li, X. Lu, W. Ding, L. Feng, Y. Gao, and Z. Guo, *Acta Crystallogr.* **64**, 702 (2008).
- [64] C. J. Bartel, C. Sutton, B. R. Goldsmith, R. Ouyang, C. B. Musgrave, L. M. Ghiringhelli, and M. Scheffler, *Sci. Adv.* **5**, eaav0693 (2019).
- [65] F. Mouhat and F.-X. Coudert, *Phys. Rev. B* **90**, 224104 (2014).
- [66] Z.-j. Wu, E.-j. Zhao, H.-p. Xiang, X.-f. Hao, X.-j. Liu, and J. Meng, *Phys. Rev. B* **76**, 054115 (2007).
- [67] R. Hill, *Proc. Phys. Soc. A* **65**, 349 (1952).
- [68] S. Pugh, London, Edinburgh Dublin Philos. Mag. J. Sci. **45**, 823 (1954).
- [69] M. Mattesini, M. Magnuson, F. Tasnádi, C. Höglund, I. A. Abrikosov, and L. Hultman, *Phys. Rev. B* **79**, 125122 (2009).
- [70] X. Liu, B. Xie, C. Duan, Z. Wang, B. Fan, K. Zhang, B. Lin, F. J. M. Colberts, W. Ma, R. A. J. Janssen, F. Huang, and Y. Cao, *J. Mater. Chem. A* **6**, 395 (2018).
- [71] X. Wang, W. Meng, and Y. Yan, *J. Appl. Phys.* **122**, 085104 (2017), <https://doi.org/10.1063/1.4991913>.
- [72] F. Ferreira, A. J. Chaves, N. M. R. Peres, and R. M. Ribeiro, *J. Opt. Soc. Am. B* **36**, 674 (2019).
- [73] S. Adhikari and P. Johari, *Phys. Rev. B* **110**, 014101 (2024).
- [74] M. Bokdam, T. Sander, A. Stroppa, S. Picozzi, D. D. Sarma, C. Franchini, and G. Kresse, *Sci. Rep.* **6**, 28618 (2016).
- [75] C. D. Spataru and F. Leonard, *Chem. Phys.* **413**, 81 (2013).
- [76] H. Fröhlich, *Adv. Phys.* **3**, 325 (1954), <https://doi.org/10.1080/00018735400101213>.
- [77] W. Shockley and H. J. Queisser, *J. Appl. Phys.* **32**, 510 (2004), [https://pubs.aip.org/aip/jap/article-pdf/32/3/510/10548356/510\\_1\\_online.pdf](https://pubs.aip.org/aip/jap/article-pdf/32/3/510/10548356/510_1_online.pdf).
- [78] A. C. Dias, M. P. Lima, and J. L. F. Da Silva, *J. Phys. Chem. C* **125**, 19142 (2021), <https://doi.org/10.1021/acs.jpcc.1c05245>.
- [79] J. Qian, B. Xu, and W. Tian, *Org. Electron.* **37**, 61 (2016).
- [80] J. Kangsabanik, V. Sugathan, A. Yadav, A. Yella, and A. Alam, *Phys. Rev. Mater.* **2**, 055401 (2018).